Inorganic Chemistry

pubs.acs.org/IC

Article

Sensitive and Reliable Fluorescent Thermometer Based on a Red-Emitting $Li_2MgHfO_4:Mn^{4+}$ Phosphor

Yonghong Qin,[¶] Fen Zhong,[¶] Yinan Bian,[¶] Shruti Hariyani, Yaxin Cao, Jakoah Brgoch, Takatoshi Seto, Mikhail G. Brik, Alok M. Srivastava, Xicheng Wang,* and Yuhua Wang

Cite This: https://doi.org/10.1021/acs.inorgchem.1c03971

Read Online

ACCESS | Metrics & More | Article Recommendations | Supporting Information

ABSTRACT: Contactless fluorescent thermometers are rapidly gaining popularity due to their sensitivity and flexibility. However, the development of sensitive and reliable non-rare-earth-containing fluorescent thermometers remains a significant challenge. Here, a new rare-earth-free, red-emitting phosphor, $Li_2MgHfO_4:Mn^{4+}$, was developed for temperature sensing. An experimental analysis combined with density functional theory and crystal field calculations reveals that the sensitive temperature-dependent luminescence arises from nonradiative transitions induced by lattice vibration. $Li_2MgHfO_4:Mn^{4+}$ also exhibits reliable recovery performance after 100 heating−cooling cycles due to the elimination of surface defects, which is rare but vital for practical application. This study puts forward a new design strategy for fluorescent thermometers and sheds light on the fundamental structure−property relationships that guide sensitive temperature-dependent luminescence. These considerations are crucial for developing next-generation fluorescence-based thermometers.

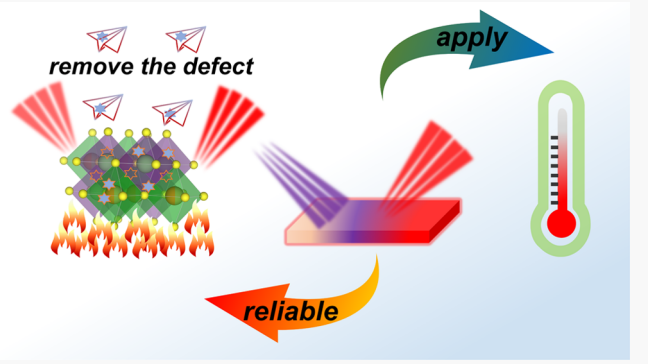

1. INTRODUCTION

The ability to measure temperature is a fundamental need for many industries, including meteorology, aerodynamics, medicine, and military technology. It also plays a pivotal role in daily life in the form of air conditioning and refrigeration.[1] Currently, reliable, inexpensive, noncontact temperature measurement technology is also sought for corrosive or hazardous environments, such as power stations or coal mines, as well as for biological and cellular applications.[2−4] Some of the most promising noncontact temperature probes available today are fluorescent thermometers, which have been utilized in bioimaging, surface temperature mapping, and scanning thermal microscopy.[5−7] Fluorescent thermometers commonly operate as optical sensors by measuring changes in the fluorescence intensity of a single or cosubstituted phosphor or monitoring the fluorescent decay lifetime dependent on temperature. The fluorescence intensity ratio (FIR) method is widely regarded as the most reliable and promising form of optical thermometry since the resulting optical properties do not depend on measurement conditions.[8,9]

Up-conversion materials with Er^{3+} and Yb^{3+} codoping like $NaYF_4:Er^{3+}/Yb^{3+}$ are among the most popular class of fluorescent thermometers. Here, relevant temperature information is provided via the ratio of the fluorescence intensity of the two activators' thermally coupled radiative transitions dependent on the temperature yield.[10−12] This material up-converts infrared (IR) light through Yb^{3+}, which undergoes energy transfer with Er^{3+} to produce green emission bands from the thermally coupled $^2H_{11/2} \rightarrow {}^4I_{15/2}$ and $^4S_{3/2} \rightarrow {}^4I_{15/2}$ transitions. Fitting the ratio of the fluorescence intensity of these two bands dependent on temperature yields a temperature sensitivity of 1.2% K^{-1}.[13] Unfortunately, these fluoride-based materials are chemically unstable in water, limiting some potential applications.[14] Research has thus turned to oxide-based up-conversion materials. One example is $Gd_2O_3:Er^{3+}/Yb^{3+}$. This material is a good fluorescent thermometer due to its maximum sensitivity of 0.0039 K^{-1} at 300 K and a minimum sensitivity of 0.0018 K^{-1} at 900 K.[15,16] The temperature information is obtained by monitoring the ratio of the emissions from two thermally coupled levels.[17] Despite the impressive thermometric optical properties, these up-conversion materials require IR excitation sources which can induce local heating, making it difficult to probe the temperature accurately.[18]

An alternative method to noncontact temperature sensing is using rare-earth or transition-metal-substituted phosphors. These phosphors can possess two thermally coupled

Received: December 21, 2021

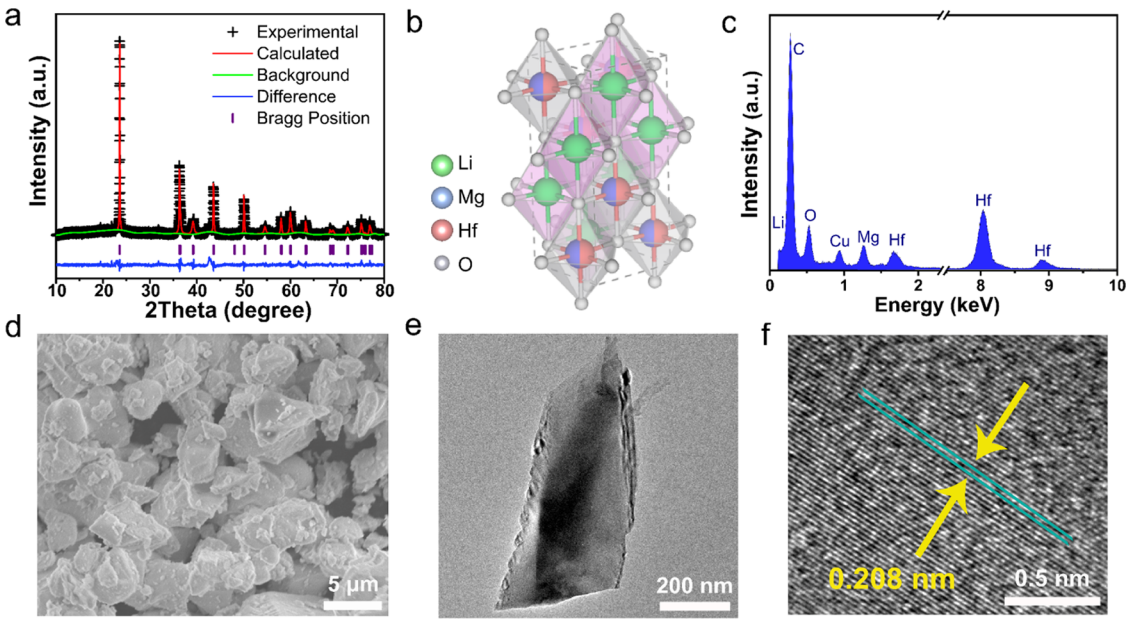

Figure 1. (a) Rietveld refinement and (b) refined crystal structure of Li_2MgHfO_4. (c) Energy-dispersive spectrum (EDS) indicates that all of the loaded elements are present in the sample. (d) SEM micrographs show that the particles have irregular morphologies. (e) TEM image and (f) HRTEM image of Li_2MgHfO_4.

transitions from a single activator, such as in $Y_2O_3:Eu^{3+}$ ($f \leftrightarrow f$ transitions with the $^5D_0$ level directly excited from specific $^7F_1$ or $^7F_2$ Stark components),[18] $Sr_2GeO_4:Pr^{3+}$ ($f \leftrightarrow f$ and $d \leftrightarrow f$ interconfigurational transitions),[19] and $Bi_2Ga_4O_9:Cr^{3+}$($d \leftrightarrow d$ transitions with $^2E/^4T_2 \rightarrow {}^4A_2$ transitions),[20] to produce fluorescent thermometers. In addition, the cosubstitution of rare-earth elements allows temperature information to be obtained from different thermal quenching performances of the activators. Examples include Eu^{2+}- and Eu^{3+}-cosubstituted Sc_2O_3 nanoparticles which produce with violet and red emission, respectively,[21] $Na_3Sc_2P_3O_{12}:Eu^{2+}$, Mn^{2+} with blue and red emissions, respectively,[22] and Ce^{3+}, Tb^{3+} codoped LaOBr with blue and green emissions, respectively.[23,24] These cosubstituted materials often rely on 4f ↔ 4f rare-earth transitions to act as the internal standard to the sensitive response of 4f ↔ 5d rare-earth transitions.

Although accurate and sensitive temperature detection is realized in both up- and down-conversion fluorescent thermometers, these materials have historically utilized rare-earth activators. The processes involved in mining, separating, and purifying the rare-earth precursors required for synthesis are intensive and linked to soil erosion and geological disasters.[25] Developing a sustainable non-rare-earth fluorescent thermometer would provide a significant value. Utilizing only transition-metal activators as a temperature probe is an alternative, cost-effective approach to noncontact temperature sensing.[26−28] To achieve this, it is imperative that the transition-metal activator is extremely sensitive to subtle changes in temperature. In addition, the emission from the transition metal must be robust to temperature cycling.[29] Any irreversible thermal degradation of the phosphor automatically inhibits accurate temperature sensing.[30] Thus, the current obstacle facing the development of next-generation, reliable, and environmentally friendly fluorescent thermometers is the identification of a sensitive and thermally robust phosphor.

In this study, we develop a rare-earth-free red-emitting phosphor, $Li_2MgHfO_4:Mn^{4+}$. This phosphor crystallizes in the rock salt crystal structure and exhibits remarkable temperature-dependent luminescence and good recovery from cycling. Density functional theory calculations revealed the structure−property relationships that influence the sensitive temperature-dependent luminescence observed in $Li_2MgHfO_4:Mn^{4+}$. This study provides a unique path to achieve next-generation fluorescent thermometers and deepens the fundamental understanding required to design luminescence-based sensors.

2. EXPERIMENTAL SECTION

2.1. Material Synthesis. The powder sample of LMH:xMn^{4+} ($0 \leq x \leq 0.5\%$) was synthesized by a high-temperature solid-state reaction. Appropriate amounts of Li_2CO_3 (99.9%), $4MgCO_3{\cdot}Mg(OH)_2{\cdot}5H_2O$ (A.R.), HfO_2 (99.9%), and MnO_2 (99.9%) were mixed and finely ground to dry in an agate mortar by adding ethanol as a dispersion medium. The powder mixture was then placed in an alumina crucible and sintered at 1250 °C for 6 h under an air atmosphere in a chamber furnace. The samples were cooled to room temperature and then reground into powders for further characterization.

2.2. Characterization. The crystal phase of the obtained sample was identified using an X-ray diffractometer (XRD, BRUKERD2 PHASER) with Cu Kα ($\lambda_{K\alpha}$ = 1.54184) radiation and operated at 30 kV and 10 mA. Rietveld refinement was implemented based on the General Structural Analysis System (GSAS) program.[31] The morphology of the sample was measured using scanning electron microscopy (SEM; Hitachi S-3600) and transmission electron microscopy (TEM, FEI Tecnai F30). TEM was also used to measure high-resolution transmission electron microscopy (HRTEM) and elemental composition (by equipped energy-dispersive X-ray (EDX) spectroscopy). The diffuse reflectance spectra (DRS) were obtained using an ultraviolet−visible (UV−vis) spectrophotometer (PE, lambda950), of which the $BaSiO_4$ white power was used as the reference. Steady-state photoluminescence (PL) and photoluminescence excitation (PLE) spectra were recorded by a fluorescence spectrophotometer (Fluorlog-3, Horiba Jobin Yvon) with a 450W xenon arc lamp as the excitation source. The temperature-dependent emission spectra were measured using the same fluorescence spectrophotometer equipped with a standard high-temperature fluorescence controller TAP-02 (Orient KOJI Instrument Co.,

https://doi.org/10.1021/acs.inorgchem.1c03971
Inorg. Chem. XXXX, XXX, XXX−XXX

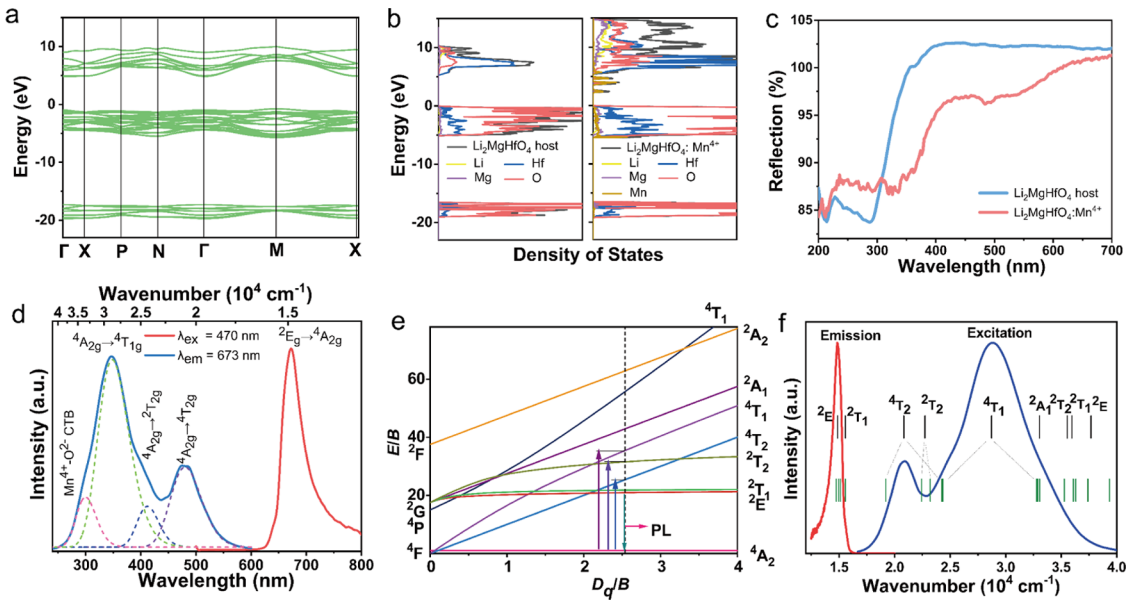

Figure 2. (a) Calculated band structure and (b) density of states of Li_2MgHfO_4. (c) Diffuse reflectance spectra of Li_2MgHfO_4 host (blue) and Li_2MgHfO_4:Mn^{4+} (LMH:Mn^{4+}, red). (d) Emission (blue) and excitation (red) spectra of Li_2MgHfO_4:Mn^{4+}. (e) Tanabe–Sugano energy-level diagram of Mn^{4+} in Li_2MgHfO_4. (f) Comparison of the experimental excitation (blue) and emission (red) spectra with the calculated Mn^{4+} energy levels of Li_2MgHfO_4:Mn^{4+}. The black and green lines represent the calculated energy levels by cubic crystal field approximation and actual symmetry, respectively.

Ltd.). The fluorescence lifetime was measured by an Edinburgh FS- 5 spectrometer.

2.3. Computational Methodology. Vienna ab initio simulation package (VASP) was used for the density functional theory (DFT) calculations employing a plane-wave basis set with projector augmented-wave (PAW) pseudopotentials.[32,33] The exchange and correlation were described using the Perdew–Burke–Ernzerhof (PBE) functional.[34] To account for the statistical site-sharing between Hf and Mg in the host structure Li_2MgHfO_4, a 1 × 1 × 1 unit cell with each possible distribution of Hf and Mg atoms was enumerated using the "Supercell software."[35] The resulting six structural models were each optimized and the most energetically favorable ordering was selected based on the lowest calculated total energy for further analysis. To determine the effect of Mn^{4+} substitution on the electronic structure of Li_2MgHfO_4, a 2 × 2 × 2 (128 atoms) supercell of the lowest energy 1 × 1 × 1 unit cell was modeled where one Hf^{4+} atom was replaced with one Mn^{4+} atom, corresponding to a 6.25% doping concentration. Each structural optimization implemented an electronic convergence criteria set to 1×10^{-8} eV and ionic relaxation set to 1×10^{-6} eV/Å. An energy cutoff of 500 eV was used and the integration of the first Brillouin zone was carried out using a Monkhorst–Pack *k*-point grid of 8 × 8 × 4 for the host structure and 6 × 6 × 2 for the Mn-doped supercell. Finally, the density of states of the host and Mn^{4+}-substituted structure as well as the band structure of the host was calculated using Heyd–Scuseria–Erzenhof screen hybrid exchange and correlation functional, HSE06, which implements a 75:25% mixture of PBE:Hartree–Fock with a range separation of 0.2 Å to correct for the significant underestimation of the PBE band gap.[36] The VASPKIT code was used for the post-processing of the VASP calculated band structure.[37]

Crystal field calculations of the Mn^{4+} energy levels were performed using two approaches: (i) cubic crystal field approximation with the above-given values of D_q, *B*, and *C* and (ii) exchange charge model of crystal field,[38−40] which does not involve any point symmetry approximation but is based on the actual symmetry of the impurity ion site. Since the details of the exchange charge model can be found in the abovementioned references, we do not give them any further details for the sake of brevity but proceed with the results of calculations.

3. RESULTS AND DISCUSSION

3.1. Phase, Crystal Structure, and Morphology. Polycrystalline samples of Li_2MgHfO_4:xMn^{4+} (x = 0, 0.001, 0.002, 0.003, 0.004, and 0.005) were synthesized through a high-temperature solid-state reaction. Rietveld refinements of the powder XRD data of the Li_2MgHfO_4 host were performed to confirm the crystal structure. As shown in Figure 1a, the refinement shows good agreement with the published crystal structure data (ICSD No. 61055).[41] The refined structural parameters are provided in Table S1, and the atomic coordinates, equivalent isotropic displacement parameters, and site occupancy factors data are summarized in Table S2. Li_2MgHfO_4 crystallizes in tetragonal space group *I*41/amd (No.141). The crystal structure, shown in Figure 1b, is composed of edge-sharing [LiO_6] and [$(Mg/Hf)O_6$] octahedra. The Mg^{2+} and Hf^{4+} cations are disordered on Wyckoff site 4a and are in a 50:50% ratio. The Li^+ ($r_{6\text{-coord}}$ = 0.76 Å), Mg^{2+} ($r_{6\text{-coord}}$ = 0.72 Å), and Hf^{4+} ($r_{6\text{-coord}}$ = 0.71 Å) cations all have similar ionic radii in octahedral coordination.[42] This makes it difficult to use size arguments to justify the substitution site for the smaller Mn^{4+} ($r_{6\text{-coord}}$ = 0.53 Å). The substitution site preference was thus investigated by calculating the bond valence sum based on the refined bond lengths.[43] According to eqs S1 and S2, the bond valence sums for the Li^+, Mg^{2+}, and Hf^{4+} sites are calculated to be 0.9208, 1.8741, and 3.4895, respectively. Since the bond valence sum of Hf^{4+} most closely resembles the oxidation state of Mn^{4+}, it could be inferred that the Mn^{4+} ions tend to occupy the Hf^{4+} site in the Li_2MgHfO_4 host crystal structure.[44] The distortion index, *D*, of [HfO_6] was then calculated to understand the local rare-earth environment further. Following eq S3, *D* is calculated to be 0.0444, indicating that the Mn^{4+} ions lie in a distorted octahedron, which agrees well with the spectroscopic properties discussed in the following section.[45]

The sample purity and morphology were further investigated using EDS and SEM. The EDS spectrum (Figure 1c) indicates

https://doi.org/10.1021/acs.inorgchem.1c03971
Inorg. Chem. XXXX, XXX, XXX−XXX

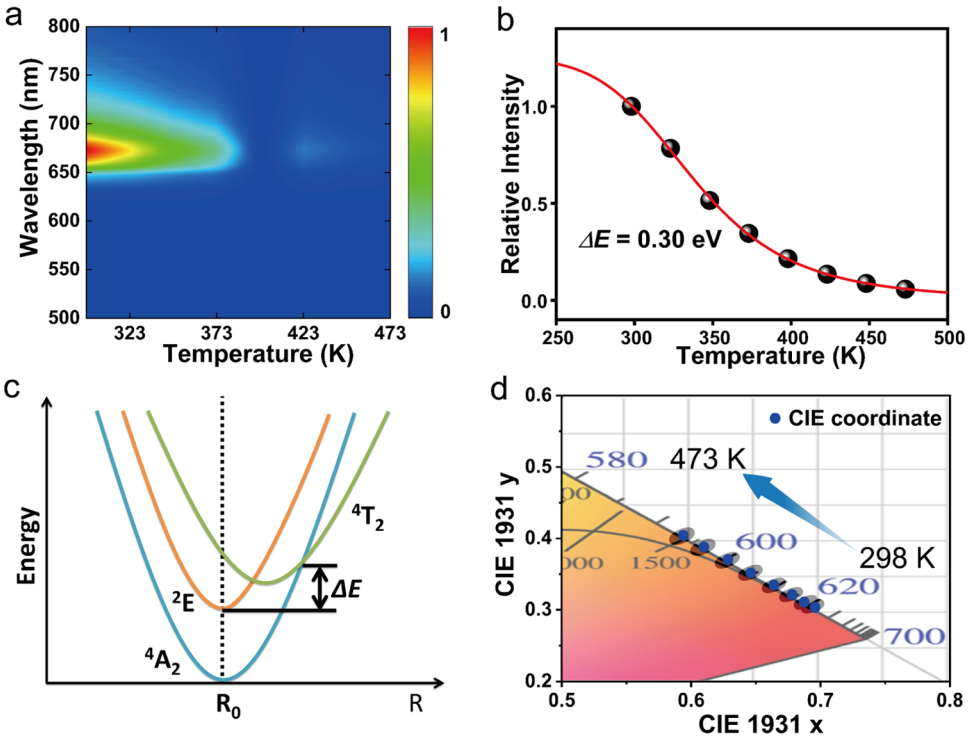

Figure 3. (a) Contour plot of the temperature-dependent emission spectra of Li_2MgHfO_4:Mn^{4+} from 298 to 473 K. (b) Relative emission intensity of Li_2MgHfO_4:Mn^{4+} as a function of temperature. The activation energy, ΔE, was determined to be 0.30 eV by fitting (red line) the emission intensity versus temperature curve to the Arrhenius equation. (c) Schematic of the mechanism of thermal quenching in Li_2MgHfO_4:Mn^{4+} and (d) 1931 CIE XYZ chromaticity coordinates (blue dots) lie within a three-step MacAdam ellipse.

that only the loaded elements, Li, Mg, Hf, and O, are present in the product. SEM also showed that the particles have irregular morphologies with particle sizes between 2 and 5 μm, as shown in the micrographs in Figure 1d and the TEM image in Figure 1e. The measured interplanar distance of Li_2MgHfO_4 was 0.208 nm, consistent with the (020) obtained from the refined structure data. These results indicate that a highly crystalline product was obtained.

Finally, the electronic structures of Li_2MgHfO_4 and Li_2MgHfO_4:Mn^{4+} were analyzed using DFT calculations. First, the hybrid band structure of Li_2MgHfO_4:Mn^{4+} was calculated to determine the value of the band gap (E_g). The calculated band structure, provided in Figure 2a, reveals an indirect band gap between Γ and M with a value of 5.58 eV. This band gap is wide enough to accommodate the 3d ↔ 3d transitions of Mn^{4+}. Decomposing the total electronic density of states into the partial density of states of Li_2MgHfO_4, as shown in Figure 2b, shows that the conduction band minimum is dominated by Hf 5d states which hybridize with O 2p states. The valence band maximum is set by O 2p states with minor contributions from the Hf 5d and Mg 3s states. Incorporating Mn^{4+} and calculating the partial density of states reveals that the conduction band minimum and valence band maximum are set by the same states as the host. The 3d states of Mn^{4+} lie within the band gap of the host crystal structure, as expected.[46]

Figure 2c displays the diffuse reflectance spectra of Li_2MgHfO_4 and Li_2MgHfO_4:Mn^{4+}. The host crystal structure exhibits high reflectance in the UV-to-visible range except for a drop between 220 and 400 nm, which is ascribed to the transition from the valence band to the conduction band of the host. The diffuse reflectance spectrum of Li_2MgHfO_4:Mn^{4+} shows more distinct absorption bands, originating from the transitions between the 3d ground state to the excited state of Mn^{4+}, which is consistent with the Mn^{4+} energy levels generated in the DOS of Li_2MgHfO_4:Mn^{4+}.[25] The experimental optical band gap of Li_2MgHfO_4 can be estimated according to eqs S4 and S5.[40] Applying the Kubelka–Munk transformation and fitting the obtained data yields a band gap value of 3.56 eV, which surprisingly is smaller than the value calculated by density functional theory (Figure S1).

3.2. Photoluminescence. The emission and excitation spectra of Li_2MgHfO_4:Mn^{4+} are presented in Figure 2d. The excitation spectrum consists of four distinct bands arising from O^{2-}-Mn^{4+} charge transfer, and $^4A_{2g}$ → $^4T_{1g}$ (~348 nm), $^4A_{2g}$ → $^2T_{2g}$ (~412 nm), and $^4A_{2g}$ → $^4T_{2g}$ (~480 nm) spin-allowed transitions, which arise from Mn^{4+} in an octahedral field.[46] The excitation spectrum also indicates that Li_2MgHfO_4:Mn^{4+} can be excited by UV (310–380 nm), near-UV (380–420 nm), and blue (420–480 nm) light, consistent with the diffuse reflectance analysis above. This phosphor shows a red emission band with the peak located at 673 nm, attributing to the ^2E_g → ^4A_g transition of Mn^{4+} in an [MnO_6] octahedral environment.[47]

Figure S2 shows the emission intensity dependence on the activator concentration of Li_2MgHfO_4:xMn^{4+} (x = 0.001, 0.002, 0.003, 0.004, and 0.005). The emission intensity maximum is obtained when x = 0.002. Therefore, all further measurements were conducted on the phosphor with this activator concentration. Further increasing the activator concentration causes the emission intensity to decrease, presumably due to the onset of concentration quenching. The low optimal activator concentration is not surprising given that concentration quenching occurs readily in these systems through energy transfer among Mn^{4+} ions.[48] The critical

https://doi.org/10.1021/acs.inorgchem.1c03971
Inorg. Chem. XXXX, XXX, XXX–XXX

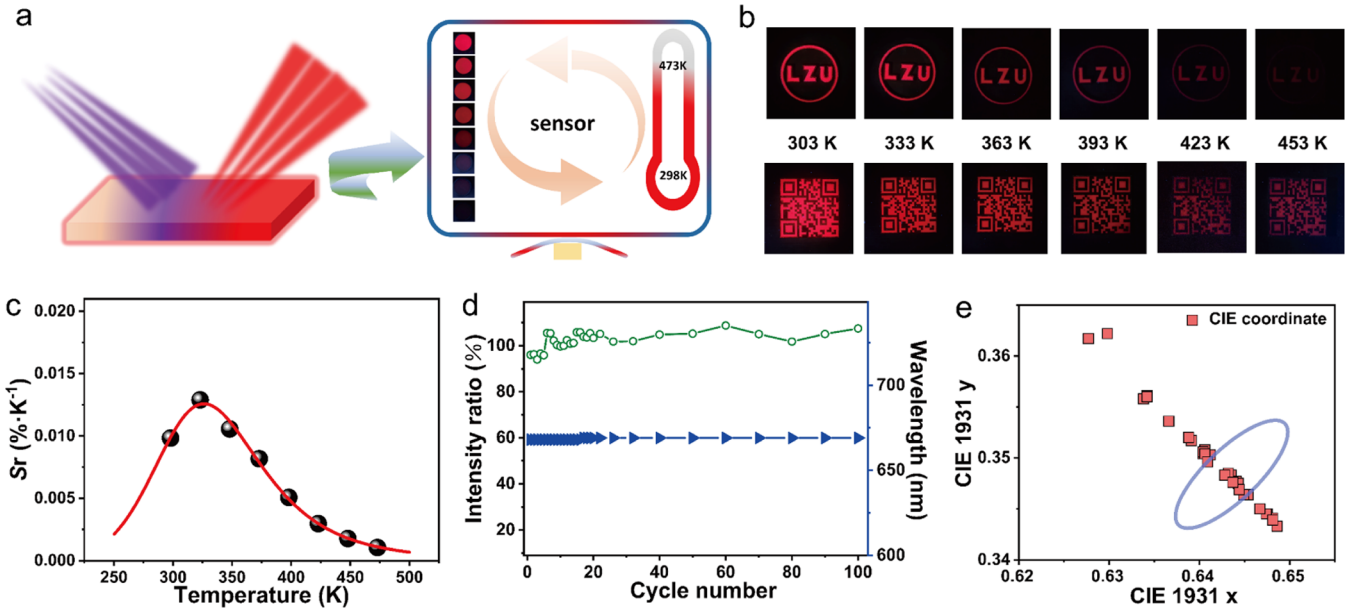

Figure 4. (a) Schematic of a sensitive and reliable fluorescent thermometer based on $Li_2MgHfO_4:Mn^{4+}$. (b) Image of LZU and a QR code illuminated by the phosphor under UV light with temperature ranging from 298 to 473 K. (c) Relative temperature-dependent sensitivity of $Li_2MgHfO_4:Mn^{4+}$. (d) Intensity ratio (green circles) and emission peak position (blue triangles) of $Li_2MgHfO_4:Mn^{4+}$ upon heating and cooling cycles. (e) 1931 CIE XYZ coordinates $Li_2MgHfO_4:Mn^{4+}$ after cycling with a three-step MacAdam ellipse drawn around the 298 K data.

distance of energy transfer, R_c, was determined using eq S6 to be 33.65 Å. The critical distance is much longer than the refined distance between the nearest-neighbor Hf^{4+} ions, 3.10 Å, making energy transfer the likely mechanism for the observed concentration quenching.

To further investigate the $3d^3$ energy level of Mn^{4+} in Li_2MgHfO_4, the Tanabe−Sugano energy-level diagram is illustrated in Figure 2e. As presented in eqs S8−S11, the corresponding wavelength and energy gap of ($^4A_{2g} \rightarrow {}^4T_{1g}$), ($^4A_{2g} \rightarrow {}^4T_{2g}$), and ($^2E_g \rightarrow {}^4A_{2g}$) transitions can be used to calculate the values of crystal field strength (D_q) and the Racah parameters B and C of Mn^{4+} Li_2MgHfO_4 as 2083, 777, and 3038 cm^{-1}, respectively. The value of D_q/B was calculated to be 2.69, which is greater than 2.2 and indicates that Mn^{4+} is in a strong crystal field environment within the host crystal structure. According to the Tanabe−Sugano energy-level diagram, the ^2E_g energy level of the d^3 electron configuration is independent of the crystal field but highly correlated to the magnitude of the nephelauxetic effect, which is related to the degree of overlap between the wavefunctions of Mn^{4+} and its surrounding ligands.[49] Brik et al. introduced a new parameter, β_1, known as the nondimensional nephalauxetic ratio, that represents a quantitative comparison of the covalent effects between host crystal structures and reflects the magnitude of the nephelauxetic effect.[50] According to eq S12, the calculated value of β_1 is 0.97, typical for oxide host crystal structures and smaller than that of fluoride hosts. This indicates a strong nephelauxetic interaction between Mn^{4+} and the surrounding O^{2-} ligands due to the less ionic nature of the Mn^{4+}−O^{2-} bonding.[51]

Crystal field calculations of the Mn^{4+} energy levels were also carried out to elucidate the energy levels of Mn^{4+} in Li_2MgHfO_4. As shown in Figure 2f and Table S5, the calculated excitation and emission energy levels show excellent agreement with the experimental spectra. Interestingly, calculations of the Mn^{4+} energy levels in actual symmetry (Mn^{4+} occupies the Hf^{4+} site with the Wyckoff 4b sites) using the following crystal field parameters (in cm^{-1}, Stevens normalization): $B_4^0 = 5135$, $B_4^4 = 31844$, $B_2^0 = -5172$, $B_2^{-1} = 7$, and $B_2^2 = -8$ show that the spin-quartet states $^4T_2$ and $^4T_1$ are widely split by the low-symmetry component of the crystal field. Such a wide splitting accounts for the broad excitation band, which was discussed above. This wide splitting could ultimately lead to sensitive temperature-dependent luminescence for reliable fluorescence thermometry.

3.3. Effect of Temperature and Cycling. Next-generation fluorescent thermometers require that the phosphor emission intensity to be extremely sensitive to changes in temperature. Thus, the temperature-dependent emission of $Li_2MgHfO_4:Mn^{4+}$ from 298 to 473 K was measured. As seen in Figure 3a, the emission intensity of $Li_2MgHfO_4:Mn^{4+}$ continually decreases with increasing temperature, likely due to increased rates of nonradiative relaxation caused by lattice vibrations.[48] By 373 K (100 °C), only 34.5% of the low-temperature emission intensity is retained. Moreover, the temperature-dependent luminescence response can be further probed by fitting the relative emission intensity data dependent on temperature to the Arrhenius equation (eq S13). The fit, seen as the red line in Figure 3b, yields an activation energy, ΔE,[52] of 0.30 eV, which is quite lower than some Mn^{4+}-doped phosphors with thermally robust luminescence ($K_2TiF_6:Mn^{4+}$—1.13 eV;[48] $K_2GeF_6:Mn^{4+}$—0.93 eV,[53] etc.). This low activation energy barrier implies that thermal quenching can readily occur, yielding highly sensitive temperature-dependent emission intensity in $Li_2MgHfO_4:Mn^{4+}$. The temperature-sensitive emission allows this material to be used as a noncontact fluorescent thermometer. This optical response is due to thermal quenching caused by the wide splitting of the $^4T_2$ and $^4T_1$ spin-quartet states of Mn^{4+} mentioned above, which can be well understood by the configuration coordinate diagram shown in Figure 3c. The lowest sublevel that arises from the $^4T_2$ state is moved closer to the emitting ^2E state, enhancing nonradiative transitions from

https://doi.org/10.1021/acs.inorgchem.1c03971
Inorg. Chem. XXXX, XXX, XXX−XXX

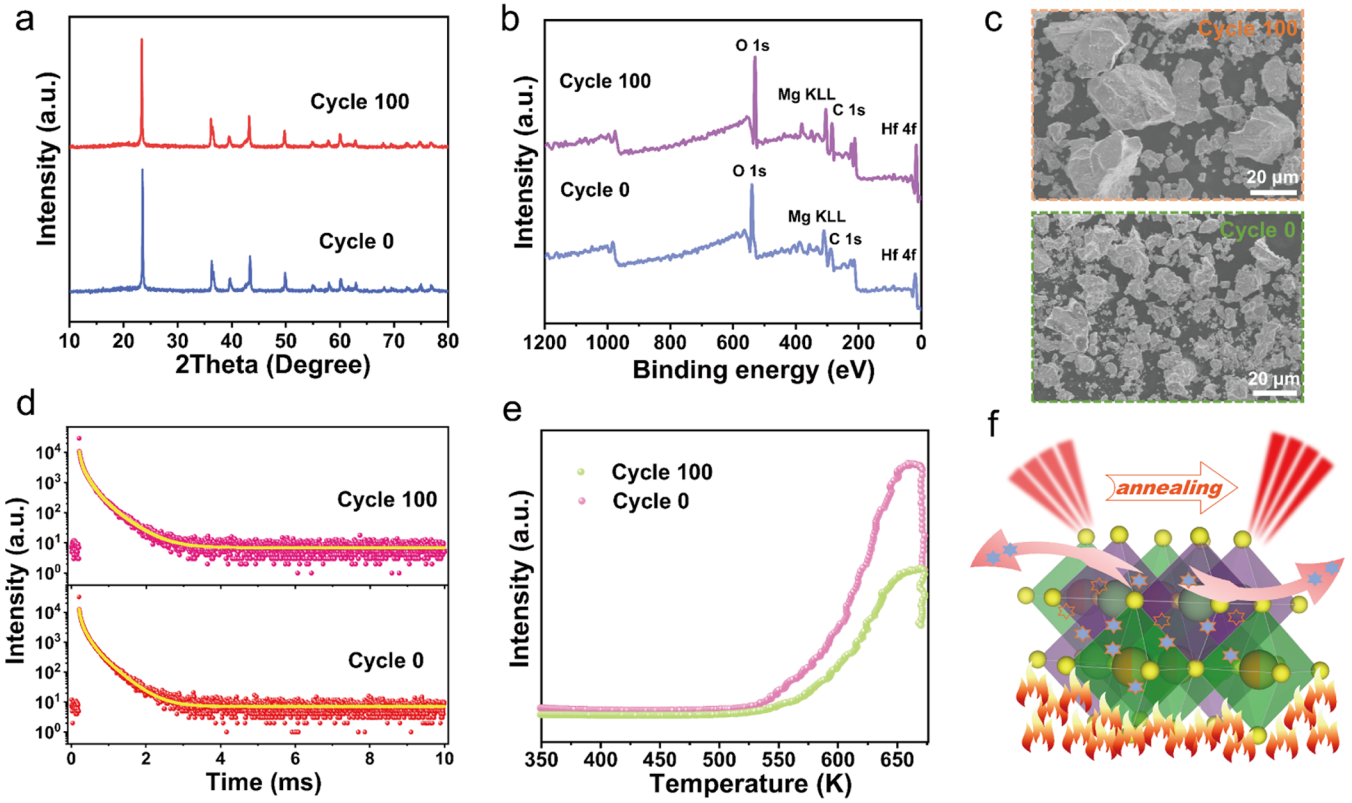

Figure 5. (a) Powder X-ray diffractograms, (b) X-ray photoelectron spectra (XPS), (c) SEM micrographs, (d) fluorescent decay curves (yellow lines are fit lines), and (e) thermoluminescence (TL) spectra of $Li_2MgHfO_4:Mn^{4+}$ before and after 100 heating and cooling cycles. (f) Schematic illustrating the mechanism for reducing defects.

the ^2E to the $^4T_2$ and ultimately back down to the $^4A_2$ ground state.[48]

Beyond the emission intensity changes, the emission color of $Li_2MgHfO_4:Mn^{4+}$ also changes depending on the temperature. As depicted in Figure 3d, the 1931 CIE XYZ chromaticity coordinates of $Li_2MgHfO_4:Mn^{4+}$ linearly shift from (0.6939, 0.3051) at 298 K to (0.5928, 0.4030) at 473 K. By analyzing the color shift via a three-step MacAdam ellipse for each of the temperature-dependent CIE coordinates, it can be observed that each ellipse is well distinguished and does not overlap, indicating that the color changes dependent on temperature are perceptible by the average human eye.[54,55] Thus, the emission color is sensitive to temperature, which is beneficial for temperature sensing applications.

The above structural and spectral characterization of $Li_2MgHfO_4:Mn^{4+}$ suggests that this phosphor is ideal for fluorescent thermometry. Thus, a schematic of a fluorescent thermometer based on $Li_2MgHfO_4:Mn^{4+}$ has been proposed in Figure 4a. This rare-earth-free phosphor exhibits a sensitive response to temperature in the range of 298−473 K where the luminescence transitions from bright red emission to fully quenched, as shown in the inset. The variation in the brightness and the perceived color of the phosphor could be standardized and calibrated to identify the temperature. An example of this is provided in Figure 4b where the fluorescence images of LZU and a QR code illuminated by the phosphor gradually become more and more unrecognizable, indicating the remarkable sensitivity of $Li_2MgHfO_4:Mn^{4+}$. The sensitivity of this phosphor is verified by calculating the relative sensitivity (S_r), a vital parameter for temperature sensors, using eq S14.[56] As displayed in Figure 4c, the relative sensitivity reaches the maximum of 0.0129 K^{-1} at 323 K in the range of 298−473 K, which is higher than the FIR-based thermometry material $NaYF_4:Er^{3+}$, Yb^{3+} (S_r = 0.012 K^{-1}),[13] indicating that $Li_2MgHfO_4:Mn^{4+}$ has excellent potential as an optical temperature sensor.

When considering the harsh operating environment of fluorescent thermometers, it is imperative to ensure that the phosphors are resistant to thermal degradation, which can cause an irreversible loss of emission intensity or luminescent lifetime and prevent a material from application. Thus, the thermal stability of $Li_2MgHfO_4:Mn^{4+}$ was investigated by conducting heating−cooling cycles from 298 to 473 K. As displayed in Figure 4d, the emission intensity remains relatively constant and fluctuates around 100% as the number of heating−cooling cycles approaches 100. Meanwhile, as shown in Figure 4d, the emission peak position of $Li_2MgHfO_4:Mn^{4+}$ remains stable after 100 heating−cooling cycles. Moreover, as shown in Figure 4e and Table S6, a number of the 1931 CIE chromaticity coordinates fall within a three-step MacAdam ellipse (0 cycle), which is also beneficial for practical applications.

To reveal the mechanism behind this serendipitous recovery behavior, systematical analyses of the structure and optical properties before and after 100 heating−cooling cycles were performed. As shown in Figure 5a, powder X-ray diffractograms are virtually identical, indicating that the average structure is not influenced by the variation in temperature. Similarly, X-ray photoelectron spectra (XPS), presented in Figure 5b, indicate that the oxidation states of the constituent elements remain unchanged after 100 temperature cycles. This recovery behavior is likely due to defects present within the

https://doi.org/10.1021/acs.inorgchem.1c03971
Inorg. Chem. XXXX, XXX, XXX−XXX

phosphor. As shown in Figure 5c, the average particle size of the material becomes larger, and the morphology is smoother after the heating−cooling process, suggesting that surface defects are reduced. This is further confirmed by fluorescence decay and thermoluminescence measurements. As shown in Figure 5d, the fluorescent decay curves were fitted (yellow line) triexponentially following eq S15. The average luminescent lifetimes were determined following eq S16 as 39.6 and 47.4 ms after 0 and 100 heating−cooling cycles, respectively. The longer luminescent lifetimes after the annealing cycles indicate that the nonradiative transitions become suppressed.[48] The morphology and decay time of $Li_2MgHfO_4:Mn^{4+}$ after six heating−cooling cycles, which is shown in Figures S3 and S4, is also consistent with this variation tendency. Meanwhile, the intensity of the thermoluminescence curve in Figure 5e decreases, indicating the number of trap states are reduced by eliminating defects.[29] A schematic of this defect-driven recovery mechanism is displayed in Figure 5f where the removal of surface defects upon annealing promotes radiative transitions and improves the resulting optical properties.

4. CONCLUSIONS

In summary, a novel non-rare-earth red-emitting phosphor, $Li_2MgHfO_4:Mn^{4+}$, was designed as a next-generation fluorescent thermometer. $Li_2MgHfO_4:Mn^{4+}$ exhibits sensitive temperature-dependent luminescence from 298 to 473 K where the relative sensitivity of the phosphor was determined to be 0.0129 K^{-1} at 323 K. Bond valence sum calculations revealed that the substituted Mn^{4+} ions tend to substitute on the Hf^{4+} site, which leads to large crystal field splitting. The structure and crystal field calculations reveal the impressive temperature-dependent optical properties originating from the nonradiative transitions induced by lattice vibration. Moreover, $Li_2MgHfO_4:Mn^{4+}$ exhibits good heating−cooling recovery performance, which results from the elimination of surface defects as confirmed by phase morphology and thermoluminescence analysis. Such recovery behavior is quite rare but vital for practical applications. This study provides a feasible guide for achieving a sensitive and reliable fluorescent thermometer and a fundamental understanding of the structure−property relationships that yield a highly responsive temperature-dependent luminescence. These results should inspire the spectral tuning of luminescence materials for a myriad of fluorescence sensing applications.

■ ASSOCIATED CONTENT

Supporting Information

The Supporting Information is available free of charge at https://pubs.acs.org/doi/10.1021/acs.inorgchem.1c03971.

Description of the crystallographic parameters of Li_2MgHfO_4, equations, optical band gap, energy transfer mechanism, calculated and experimental energy levels for Mn^{4+} in Li_2MgHfO_4, CIE coordinates of $Li_2MgHfO_4:Mn^{4+}$ dependent on heating−cooling cycle numbers, morphology, and fluorescent decay of $Li_2MgHfO_4:Mn^{4+}$ after six heating−cooling cycles (PDF)

■ AUTHOR INFORMATION

Corresponding Author

Xicheng Wang − *School of Materials and Energy, Lanzhou University, Lanzhou 730000, China; National & Local Joint Engineering Laboratory for Optical Conversion Materials and Technology and Key Laboratory for Special Function Materials and Structural Design of the Ministry of the Education, Lanzhou University, Lanzhou 730000, China;* orcid.org/0000-0002-4310-5967; Email: wangxc@lzu.edu.cn

Authors

Yonghong Qin − *School of Materials and Energy, Lanzhou University, Lanzhou 730000, China; National & Local Joint Engineering Laboratory for Optical Conversion Materials and Technology and Key Laboratory for Special Function Materials and Structural Design of the Ministry of the Education, Lanzhou University, Lanzhou 730000, China*

Fen Zhong − *School of Materials and Energy, Lanzhou University, Lanzhou 730000, China; National & Local Joint Engineering Laboratory for Optical Conversion Materials and Technology and Key Laboratory for Special Function Materials and Structural Design of the Ministry of the Education, Lanzhou University, Lanzhou 730000, China*

Yinan Bian − *School of Materials and Energy, Lanzhou University, Lanzhou 730000, China; National & Local Joint Engineering Laboratory for Optical Conversion Materials and Technology and Key Laboratory for Special Function Materials and Structural Design of the Ministry of the Education, Lanzhou University, Lanzhou 730000, China*

Shruti Hariyani − *Department of Chemistry, University of Houston, Houston 77204 Texas, United States*

Yaxin Cao − *School of Materials and Energy, Lanzhou University, Lanzhou 730000, China; National & Local Joint Engineering Laboratory for Optical Conversion Materials and Technology and Key Laboratory for Special Function Materials and Structural Design of the Ministry of the Education, Lanzhou University, Lanzhou 730000, China*

Jakoah Brgoch − *Department of Chemistry, University of Houston, Houston 77204 Texas, United States;* orcid.org/0000-0002-1406-1352

Takatoshi Seto − *School of Materials and Energy, Lanzhou University, Lanzhou 730000, China*

Mikhail G. Brik − *College of Sciences & CQUPT-BUL Innovation Institute, Chongqing University of Posts and Telecommunications, Chongqing 400065, People's Republic of China; Institute of Physics, University of Tartu, Tartu 50411, Estonia; Institute of Physics, Jan Długosz University, PL-42200 Częstochowa, Poland; Academy of Romanian Scientists, 050044 Bucharest, Romania*

Alok M. Srivastava − *Current Lighting Solutions, LLC, Cleveland, Ohio 44110, United States*

Yuhua Wang − *School of Materials and Energy, Lanzhou University, Lanzhou 730000, China; National & Local Joint Engineering Laboratory for Optical Conversion Materials and Technology and Key Laboratory for Special Function Materials and Structural Design of the Ministry of the Education, Lanzhou University, Lanzhou 730000, China;* orcid.org/0000-0001-7047-4760

Complete contact information is available at: https://pubs.acs.org/10.1021/acs.inorgchem.1c03971

https://doi.org/10.1021/acs.inorgchem.1c03971
Inorg. Chem. XXXX, XXX, XXX−XXX

Author Contributions

[¶]Y.Q., F.Z., and Y.B. contributed equally to this work.

Notes

The authors declare no competing financial interest.

■ ACKNOWLEDGMENTS

This work was supported by the National Natural Science Foundation of China (Nos. 51902147 and U1905213), the Science and Technology Projects of Gansu Province (No. 20JR5RA218), and the National College Student Innovation and Entrepreneurship Training Program in 2019 (No. 201910730115). M.G. Brik thanks the supports from the Programme for the Foreign Experts (Grant No. W2017011) and Wenfeng High-end Talents Project (Grant No. W2016-01) offered by the Chongqing University of Posts and Telecommunications (CQUPT), the Estonian Research Council grant PUT PRG111, the European Regional Development Fund (TK141), and NCN project 2018/31/B/ST4/00924. S.H. and J.B. acknowledge funding from the National Science Foundation (CER-1911311) and the Welch Foundation (E-1981). This work used the Optunita/Sabine/Carya cluster(s) operated by the Research Computing Data Core at the University of Houston.

■ REFERENCES

(1) Wang, X.-d.; Wolfbeis, O. S.; Meier, R. J. Luminescent probes and sensors for temperature. *Chem. Soc. Rev.* **2013**, *42*, 7834−7869.

(2) Hsiao, W. W. W.; Hui, Y. Y.; Tsai, P. C.; Chang, H. C. Fluorescent Nanodiamond: A Versatile Tool for Long-Term Cell Tracking, Super-Resolution Imaging, and Nanoscale Temperature Sensing. *Acc. Chem. Res.* **2016**, *49*, 400−407.

(3) Cui, Y. J.; Zhu, F. L.; Chen, B. L.; Qian, G. D. Metal-organic frameworks for luminescence thermometry. *ChemComm.* **2015**, *51*, 7420−7431.

(4) Kucsko, G.; Maurer, P. C.; Yao, N. Y.; Kubo, M.; Noh, H. J.; Lo, P. K.; Park, H.; Lukin, M. D. Nanometre-scale thermometry in a living cell. *Nature* **2013**, *500*, 54−58.

(5) Shinde, S. L.; Nanda, K. K. Wide-Range Temperature Sensing using Highly Sensitive Green-Luminescent ZnO and PMMA-ZnO Film as a Non-Contact Optical Probe. *Angew. Chem., Int. Ed.* **2013**, *52*, 11325−11328.

(6) Yakunin, S.; Benin, B. M.; Shynkarenko, Y.; Nazarenko, O.; Bodnarchuk, M. I.; Dirin, D. N.; Hofer, C.; Cattaneo, S.; Kovalenko, M. V. High-resolution remote thermometry and thermography using luminescent low-dimensional tin-halide perovskites. *Nat. Mater.* **2019**, *18*, 846−852.

(7) Quintanilla, M.; Liz-Marzan, L. M. Guiding Rules for Selecting a Nanothermometer. *Nano Today* **2018**, *19*, 126−145.

(8) Zhang, D.; Xu, Y.; Liu, Q.; Xia, Z. Encapsulation of $CH_3NH_3PbBr_3$ Perovskite Quantum Dots in MOF-5 Microcrystals as a Stable Platform for Temperature and Aqueous Heavy Metal Ion Detection. *Inorg. Chem.* **2018**, *57*, 4613−4619.

(9) Hu, T.; Gao, Y.; Molokeev, M.; Xia, Z.; Zhang, Q. Non-stoichiometry in $Ca_2Al_2SiO_7$ enabling mixed-valent europium toward ratiometric temperature sensing. *Sci. China Mater.* **2019**, *62*, 1807−1814.

(10) Rodríguez-Sevilla, P.; Zhang, Y.; Haro-González, P.; Sanz-Rodríguez, F.; Jaque, F.; Solé, J. G.; Liu, X.; Jaque, D. Thermal Scanning at the Cellular Level by an Optically Trapped Upconverting Fluorescent Particle. *Adv. Mater.* **2016**, *28*, 2421−2426.

(11) Mi, C.; Zhou, J.; Wang, F.; Lin, G.; Jin, D. Ultrasensitive Ratiometric Nanothermometer with Large Dynamic Range and Photostability. *Chem. Mater.* **2019**, *31*, 9480−9487.

(12) Cerón, E. N.; Ortgies, D. H.; del Rosal, B.; Ren, F.; Benayas, A.; Vetrone, F.; Ma, D.; Sanz-Rodríguez, F.; Solé, J. G.; Jaque, D.; Rodríguez, E. M. Hybrid Nanostructures for High-Sensitivity Luminescence Nanothermometry in the Second Biological Window. *Adv. Mater.* **2015**, *27*, 4781−4787.

(13) Zhou, S.; Deng, K.; Wei, X.; Jiang, G.; Duan, C.; Chen, Y.; Yin, M. Upconversion luminescence of $NaYF_4$: Yb^{3+}, Er^{3+} for temperature sensing. *Opt. Commun.* **2013**, *291*, 138−142.

(14) Himmelstoß, S. F.; Hirsch, T. Long-Term Colloidal and Chemical Stability in Aqueous Media of $NaYF_4$-Type Upconversion Nanoparticles Modified by Ligand-Exchange. *Part. Part. Syst. Charact.* **2019**, *36*, No. 1900235.

(15) Vetrone, F.; Naccache, R.; Zamarron, A.; de la Fuente, A. J.; Sanz-Rodriguez, F.; Maestro, L. M.; Rodriguez, E. M.; Jaque, D.; Sole, J. G.; Capobianco, J. A. Temperature Sensing Using Fluorescent Nanothermometers. *ACS Nano* **2010**, *4*, 3254−3258.

(16) Singh, S. K.; Kumar, K.; Rai, S. B. Er^{3+}/Yb^{3+} codoped Gd_2O_3 nano-phosphor for optical thermometry. *Sens. Actuator, A* **2009**, *149*, 16−20.

(17) Brites, C. D. S.; Xie, X. J.; Debasu, M. L.; Qin, X.; Chen, R. F.; Huang, W.; Rocha, J.; Liu, X. G.; Carlos, L. D. Instantaneous ballistic velocity of suspended Brownian nanocrystals measured by upconversion nanothermometry. *Nat. Nanotechnol.* **2016**, *11*, 851.

(18) Souza, A. S.; Nunes, L. A. O.; Silva, I. G. N.; Oliveira, F. A. M.; da Luz, L. L.; Brito, H. F.; Felinto, M. C. F. C.; Ferreira, R. A. S.; Júnior, S. A.; Carlos, L. D.; Malta, O. L. Highly-sensitive Eu^{3+} ratiometric thermometers based on excited state absorption with predictable calibration. *Nanoscale* **2016**, *8*, 5327−5333.

(19) Brites, C. D. S.; Fiaczyk, K.; Ramalho, J. F. C. B.; Sójka, M.; Carlos, L. D.; Zych, E. Widening the Temperature Range of Luminescent Thermometers through the Intra- and Interconfigurational Transitions of Pr^{3+}. *Adv. Opt. Mater.* **2018**, *6*, No. 1701318.

(20) Back, M.; Trave, E.; Ueda, J.; Tanabe, S. Ratiometric Optical Thermometer Based on Dual Near-Infrared Emission in Cr^{3+}-Doped Bismuth-Based Gallate Host. *Chem. Mater.* **2016**, *28*, 8347−8356.

(21) Pan, Y.; Xie, X.; Huang, Q.; Gao, C.; Wang, Y.; Wang, L.; Yang, B.; Su, H.; Huang, L.; Huang, W. Inherently Eu^{2+}/Eu^{3+} Codoped Sc_2O_3 Nanoparticles as High-Performance Nanothermometers. *Adv. Mater.* **2018**, *30*, No. 1705256.

(22) Zhang, X. G.; Zhu, Z. P.; Guo, Z. Y.; Sun, Z. S.; Chen, Y. B. A ratiometric optical thermometer with high sensitivity and superior signal discriminability based on $Na_3Sc_2P_3O_{12}$: Eu^{2+}, Mn^{2+} thermochromic phosphor. *Chem. Eng. J.* **2019**, *356*, 413−422.

(23) Zhang, X.; Huang, Y.; Gong, M. Dual-emitting Ce^{3+}, Tb^{3+} co-doped LaOBr phosphor: Luminescence, energy transfer and ratiometric temperature sensing. *Chem. Eng. J.* **2017**, *307*, 291−299.

(24) Wang, Q.; Liao, M.; Lin, Q.; Xiong, M.; Mu, Z.; Wu, F. A review on fluorescence intensity ratio thermometer based on rare-earth and transition metal ions doped inorganic luminescent materials. *J. Alloys Compd.* **2021**, *850*, No. 156744.

(25) Zhu, H. M.; Lin, C. C.; Luo, W. Q.; Shu, S. T.; Liu, Z. G.; Liu, Y. S.; Kong, J. T.; Ma, E.; Cao, Y. G.; Liu, R. S.; Chen, X. Y. Highly efficient non-rare-earth red emitting phosphor for warm white light-emitting diodes. *Nat. Commun.* **2014**, *5*, No. 4312.

(26) Li, F.; Cai, J.; Chi, F.; Chen, Y.; Duan, C.; Yin, M. Investigation of luminescence from LuAG: Mn $^{4+}$ for physiological temperature sensing. *Opt. Mater.* **2017**, *66*, 447−452.

(27) Cai, P.; Qin, L.; Chen, C.; Wang, J.; Bi, S.; Kim, S. I.; Huang, Y.; Seo, H. J. Optical Thermometry Based on Vibration Sidebands in Y_2MgTiO_6:Mn^{4+} Double Perovskite. *Inorg. Chem.* **2018**, *57*, 3073−3081.

(28) Chen, Y.; He, J.; Zhang, X.; Rong, M.; Xia, Z.; Wang, J.; Liu, Z. Q. Dual-Mode Optical Thermometry Design in $Lu_3Al_5O_{12}$:Ce^{3+}/Mn^{4+} Phosphor. *Inorg. Chem.* **2020**, *59*, 1383−1392.

(29) Kim, Y. H.; Arunkumar, P.; Kim, B. Y.; Unithrattil, S.; Kim, E.; Moon, S. H.; Hyun, J. Y.; Kim, K. H.; Lee, D.; Lee, J. S.; Im, W. B. A zero-thermal-quenching phosphor. *Nat. Mater.* **2017**, *16*, 543.

(30) Yeh, C.-W.; Chen, W.-T.; Liu, R.-S.; Hu, S.-F.; Sheu, H.-S.; Chen, J.-M.; Hintzen, H. T. Origin of Thermal Degradation of $Sr_{2-x}Si_5N_8$:Eu_x Phosphors in Air for Light-Emitting Diodes. *J. Am. Chem. Soc.* **2012**, *134*, 14108−14117.

https://doi.org/10.1021/acs.inorgchem.1c03971
Inorg. Chem. XXXX, XXX, XXX−XXX

(31) Larson, A. C.; Von Dreele, R. B. *Generalized Crystal Structure Analysis System*; University of California, 1988.
(32) Kresse, G.; Furthmüller, J. Efficient iterative schemes for ab initio total-energy calculations using a plane-wave basis set. *Phys. Rev. B: Condens. Matter Mater. Phys.* **1996**, *54*, 11169−11186.
(33) Kresse, G.; Joubert, D. From ultrasoft pseudopotentials to the projector augmented-wave method. *Phys. Rev. B: Condens. Matter Mater. Phys.* **1999**, *59*, 1758−1775.
(34) Blöchl, P. E. Projector augmented-wave method. *Phys. Rev. B: Condens. Matter Mater. Phys.* **1994**, *50*, 17953−17979.
(35) Okhotnikov, K.; Charpentier, T.; Cadars, S. Supercell program: a combinatorial structure-generation approach for the local-level modeling of atomic substitutions and partial occupancies in crystals. *J. Cheminformatics* **2016**, *8*, No. 17.
(36) Heyd, J.; Scuseria, G. E.; Ernzerhof, M. Hybrid functionals based on a screened Coulomb potential. *J. Chem. Phys.* **2003**, *118*, 8207−8215.
(37) Wang, V.; Xu, N.; Liu, J.-C.; Tang, G.; Geng, W.-T. VASPKIT: A User-Friendly Interface Facilitating High-Throughput Computing and Analysis Using VASP Code. *Comput. Phys. Commun.* **2021**, *267*, No. 108033.
(38) Brik, M.; Srivastava, A. Comparative crystal field analysis of energy level schemes and nephelauxetic effect for Cr^{4+}, Cr^{3+}, and Mn^{4+} ions in $Y_2Sn_2O_7$ pyrochlore. *Opt. Mater.* **2013**, *35*, 1251−1256.
(39) Brik, M. G.; Ma, C.-G. *Theoretical Spectroscopy of Transition Metal and Rare Earth Ions: From Free State to Crystal Field*; Jenny Stanford Publishing, 2019.
(40) Kaplyanskii, A. A.; B M M E *Spectroscopy of Solids Containing Rare Earth Ions*; Elsevier Science Publishers B.V.: North-Holland, Amsterdam, 1987.
(41) Castellanos, M.; West, A. R.; Reid, W. B. Dilithium magnesium zirconium tetraoxide with an [alpha]-$LiFeO_2$ structure. *Acta Crystallogr. Sect. C.* **1985**, *41*, 1707−1709.
(42) Shannon, R. Revised effective ionic radii and systematic studies of interatomic distances in halides and chalcogenides. *Acta Crystallogr. Sect. A.* **1976**, *32*, 751−767.
(43) Brown, I. D.; Altermatt, D. Bond-valence Parameters Obtained From A Systematic Analysis Of The Inorganic Crystal-structure Database. *Acta Crystallogr., Sect. B: Struct. Sci.* **1985**, *41*, 244−247.
(44) Zhang, Y.; Li, X.; Li, K.; Lian, H.; Shang, M.; Lin, J. Crystal-Site Engineering Control for the Reduction of Eu^{3+} to Eu^{2+} in $CaYAlO_4$: Structure Refinement and Tunable Emission Properties. *ACS Appl. Mater. Interfaces* **2015**, *7*, 2715−2725.
(45) Cozzan, C.; Laurita, G.; Gaultois, M. W.; Cohen, M.; Mikhailovsky, A. A.; Balasubramanian, M.; Seshadri, R. Understanding the links between composition, polyhedral distortion, and luminescence properties in green-emitting beta-$Si_{6-z}Al_zO_zN_{8-z}$:Eu^{2+} phosphors. *J. Mater. Chem. C* **2017**, *5*, 10039−10046.
(46) Wang, B.; Lin, H.; Huang, F.; Xu, J.; Chen, H.; Lin, Z. B.; Wang, Y. S. Non-Rare-Earth $BaMgAl_{10-2x}O_{17}$:xMn^{4+},xMg^{2+}: A Narrow-Band Red Phosphor for Use as a High-Power Warm w-LED. *Chem. Mater.* **2016**, *28*, 3515−3524.
(47) Li, K.; Du, J.; Poelman, D.; Vrielinck, H.; Mara, D.; Van Deun, R. Achieving Efficient Red-Emitting $Sr_2Ca_{1-\delta}Ln_\delta WO_6$:$Mn^{4+}$ (Ln = La, Gd, Y, Lu, δ = 0.10) Phosphors with Extraordinary Luminescence Thermal Stability for Potential UV-LEDs Application via Facile Ion Substitution in Luminescence-Ignorable Sr_2CaWO_6:Mn^{4+}. *ACS Mater. Lett.* **2020**, *2*, 771−778.
(48) Senden, T.; van Dijk-Moes, R. J. A.; Meijerink, A. Quenching of the red Mn^{4+} luminescence in Mn^{4+}-doped fluoride LED phosphors. *Light: Sci. Appl.* **2018**, *7*, No. 8.
(49) Kim, M.; Park, W. B.; Lee, J.-W.; Lee, J.; Kim, C. H.; Singh, S. P.; Sohn, K.-S. Rb_3SiF_7:Mn^{4+} and Rb_2CsSiF_7:Mn^{4+} Red-Emitting Phosphors with a Faster Decay Rate. *Chem. Mater.* **2018**, *30*, 6936−6944.
(50) Brik, M. G.; Srivastava, A. M. Electronic Energy Levels of the Mn^{4+} Ion in the Perovskite, $CaZrO_3$. *ECS J. Solid State Sci. Technol.* **2013**, *2*, R148−R152.
(51) Brik, M.; Camardello, S. J.; Srivastava, A. Influence of Covalency on the Mn^{4+} 2Eg→4A2g Emission Energy in Crystals. *ECS J. Solid State Sci. Technol.* **2015**, *4*, R39−R43.
(52) Lin, C. C.; Tsai, Y.-T.; Johnston, H. E.; Fang, M.-H.; Yu, F.; Zhou, W.; Whitfield, P.; Li, Y.; Wang, J.; Liu, R.-S.; Attfield, J. P. Enhanced Photoluminescence Emission and Thermal Stability from Introduced Cation Disorder in Phosphors. *J. Am. Chem. Soc.* **2017**, *139*, 11766−11770.
(53) Wei, L.-L.; Lin, C. C.; Wang, Y.-Y.; Fang, M.-H.; Jiao, H.; Liu, R.-S. Photoluminescent Evolution Induced by Structural Transformation Through Thermal Treating in the Red Narrow-Band Phosphor K_2GeF_6:Mn^{4+}. *ACS Appl. Mater. Interfaces* **2015**, *7*, 10656−10659.
(54) Zhuo, Y.; Hariyani, S.; Zhong, J.; Brgoch, J. Creating a Green-Emitting Phosphor through Selective Rare-Earth Site Preference in $NaBaB_9O_{15}$:Eu^{2+}. *Chem. Mater.* **2021**, *33*, 3304−3311.
(55) Chickering, K. FMC color-difference formulas: Clarification concerning usage. *JOSA* **1971**, *61*, 118−122.
(56) Chi, F.; Jiang, B.; Zhao, Z.; Chen, Y.; Wei, X.; Duan, C.; Yin, M.; Xu, W. Multimodal temperature sensing using Zn_2GeO_4:Mn^{2+} phosphor as highly sensitive luminescent thermometer. *Sens. Actuators, B* **2019**, *296*, No. 126640.

https://doi.org/10.1021/acs.inorgchem.1c03971
Inorg. Chem. XXXX, XXX, XXX−XXX